Broadband Compact Silicon Wire to Silicon Slot Waveguide Orthogonal Bend

Herman M. K. Wong, Charles Lin, Mohamed A. Swillam, *Senior Member, IEEE*, and Amr S. Helmy, *Senior Member, IEEE*

***Abstract*—An ultra-compact 90° bend between silicon (Si) wire and silicon slot waveguide (SSW) with a footprint of ∼725 nm × 500 nm is experimentally demonstrated on silicon-on-insulator substrate. By achieving momentum matching of the waveguides through an orthogonal junction placement, and maximizing modal overlap through an angled facet, coupling efficiency of ∼70% and 3-dB bandwidth of over 500 nm has been achieved. The nominal experimental transmission through cascaded input (Si wire to SSW) and output (SSW to Si wire) orthogonal junctions match closely those obtained from simulations, both in the range from 1270 to 1360 nm and from 1480 to 1590 nm. For slot widths ranging from 30 to 230 nm, our Si wire-SSW bend can achieve coupling efficiency comparable to that of a direct butt-coupler over a 400 nm bandwidth. This compact and wideband waveguide bend serves as an important component to enable dense integration between conventional Si wire and SSW.**

***Index Terms*—Integrated optics, silicon photonics, slot waveguide.**

I. Introduction

NANOPHOTONIC devices in the well developed silicon (Si) platform have attracted increasing attention. They allow for large-scale, lower-cost optoelectronic integration that can benefit a host of important applications such as sensing, optical communications, and computing systems. Recently, the Si slot waveguide (SSW), which guides an appreciable portion of the EM field in the low index slot region between two adjacent Si claddings, has emerged as a promising candidate for nanophotonic devices [1]. SSWs offer more flexibility over traditional Si wire waveguides due to the enhanced light–matter interaction within the subwavelength slot. For example, the appreciable field confinement within the slot leads to a reduction in the optical power required to invoke optical nonlinear effects. Nonlinear processes such as ultrafast all-optical switching [2] and optical modulation and detection [3] based on SSWs have been demonstrated. Moreover, with enormous optical intensity confined within the nanoscale slot region, it is also possible to utilize SSWs for sensing applications [4] as well as optical trapping and manipulation of nano-particles [5].

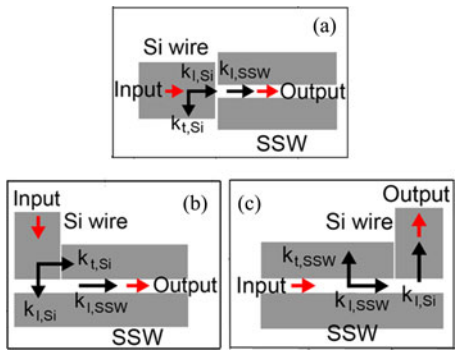

Fig. 1. Schematics of (a) the parallel coupling configuration from Si wire to SSW, (b) the orthogonal coupling configuration from Si wire to SSW, and (c) the orthogonal coupling configuration from SSW to Si wire.

Despite these versatile attributes, SSWs have propagation loss on the order of 10 dB/cm [6], which is significantly higher than the loss of 1 dB/cm in the case of Si wire waveguides [7]. Thus, to reduce insertion loss while achieving high performance and compactness, it is advantageous to integrate the two types of waveguides for photonic device design. This will require an efficient and ultra-compact means of routing and coupling light between Si wires and SSWs with minimum footprint on the chip.

In the case of butt coupling (parallel configuration) between silicon wire and SSW (Fig. 1(a)), a taper structure can be introduced between them to increase the coupling efficiency; and previous works have demonstrated up to 97% coupling efficiency over a broad wavelength range [8]–[11]. However, the length of the taper required is, for example, 8 μm for 97% coupling efficiency [10] and 5 μm for 83% [11]. Thus, the footprint of these couplers is comparable to that of the devices they are designed to couple in and out of, thus setting an upper bound for on-chip device integration density.

In addition, in recent years, great efforts have been dedicated to increase the compatibility of silicon photonics with the standard CMOS fabrication process. In order to have electronic and photonic devices coexisting on the same chip, one challenge is the ability to utilize sharp bends for photonic devices as it is for electronics. This will dramatically reduce the footprint, and thus allow for more devices to be integrated on the same chip. However, photonic devices that are based on total internal reflection guiding approaches have mainly adiabatic structures

Manuscript received July 26, 2013; revised November 14, 2013; accepted February 3, 2014. Date of publication February 10, 2014; date of current version March 7, 2014. This work was supported in part by CMC Microsystems.

H. M. K. Wong, C. Lin, and A. S. Helmy are with the Department of Electrical and Computer Engineering, University of Toronto, Toronto, ON M5S 3G4, Canada (e-mail: herman.wong@mail.utoronto.ca; charleschihchin.lin@mail.utoronto.ca; a.helmy@utoronto.ca).

M. A. Swillam was with the Department of Electrical and Computer Engineering, University of Toronto, Toronto, ON M5S 3G4, Canada, and is now with the Department of Physics, American University in Cairo, New Cairo 11835, Egypt (e-mail: m.swillam@aucegypt.edu).

Color versions of one or more of the figures in this paper are available online at http://ieeexplore.ieee.org.

Digital Object Identifier 10.1109/JLT.2014.2305661

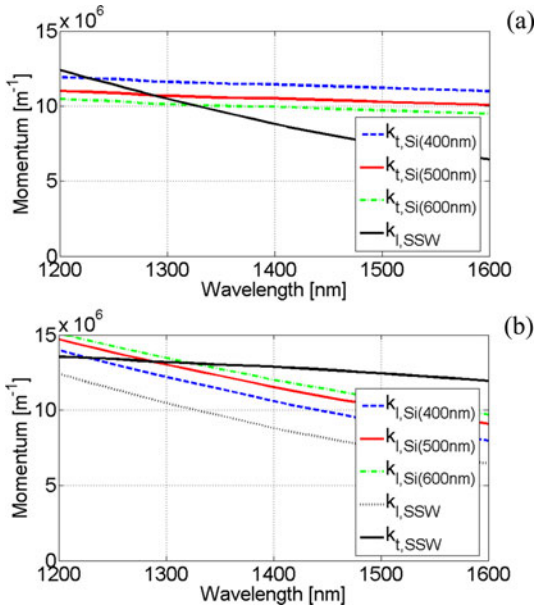

Fig. 2. Plots of the relevant light momentum components as a function of wavelength for (a) the orthogonal bend from Si wire to SSW, and (b) the orthogonal bend from SSW to Si wire and the parallel coupler (light momenta for Si wire waveguides of different widths are plotted).

for bends to avoid radiation losses. For example, it is shown by simulation in [12] that SSW bend loss can be reduced by shifting the location of the slot region to be closer to the outside of the bend. However, in a 1 μm radius 90° bend, the bend loss is approximately 20%; only when the bend radius is increased to 5 μm does the loss become negligible. In [13], it is shown that bend loss in a silicon wire waveguide can be significantly reduced by improving the waveguide profile through optimized etch chemistry. However, to achieve a negligible bend loss, a bend radius of 2 μm is required, and the propagation loss is adversely increased by the change in waveguide profile.

In this work, we report the design, fabrication, and characterization of a Si wire– SSW 90° sharp bend that has good coupling efficiency over a wide wavelength range and sub-micrometer footprint. It will be shown using numerical simulations and confirmed experimentally that the orthogonal placement of the two waveguides (Fig. 1(b)) can help satisfy the momentum matching condition and thus lead to sufficient energy transfer without the need for an extended taper, thus achieving the goal to trade off some of the coupling efficiency for ultra-compactness.

II. Design of the Silicon Wire to SSW Bend

In our proposed design, momentum matching between the two waveguides is established by cascading the Si wire and the SSW in a 90° junction (see Fig. 1(b)). Such orthogonal coupling technique has previously been experimentally demonstrated for ultra-wideband coupling from Si wire to plasmonic slot waveguides [14], [15]. When the Si wire and SSW are placed in a parallel fashion (see Fig. 1(a)), there exists significant mismatch over all wavelengths between $k_{\mathrm{l,Si}}$, the longitudinal momentum component of the Si wire, and $k_{\mathrm{l,SSW}}$, the longitudinal momentum component of the SSW (see Fig. 2(b)). Thus, extended

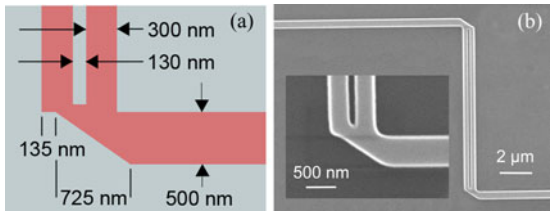

Fig. 3. (a) Schematic of the Si wire to SSW orthogonal bend; the length of the angled facet is 725 nm and the offset with respect to the outer cladding of the SSW is 135 nm. (b) SEM image of the Si wire to SSW orthogonal coupling platform for the 10 μm long SSW. Inset: SEM image of one orthogonal bend junction. The thickness of the Si layer is 220 nm.

taper structures are necessary to enhance energy transfer. On the other hand, when the two waveguides are placed in an orthogonal fashion, $k_{t,\mathrm{Si}}$, the transverse momentum component of the Si wire, is of more importance for the waveguide coupling. In this configuration, the momentum mismatch reduces significantly in comparison with that of the parallel configuration from 1200 to 1500 nm, and even intersects at a specific wavelength, which represents the wavelength where coupling efficiency is maximized due to zero momentum mismatch (see Fig. 2(a)). This means that broadband energy transfer can be readily obtained. By adjusting the width of the Si wire, the momentum matching condition can be tuned to specific wavelengths. Moreover, we see that the orthogonal junction scheme also helps in reducing the momentum mismatch when light is propagating from the SSW into the Si wire. In this case, $k_{t,\mathrm{SSW}}$ and $k_{\mathrm{l,Si}}$ are the components utilized for momentum matching (see Fig. 1(c)). It can be observed that the location of the momentum matching condition is preserved and the mismatch is minimal over a large spectrum regardless of the EM wave's direction of propagation (see Fig. 2(b)).

In addition to creating orthogonal placement to achieve momentum matching, the Si wire also needs to be angled near the junction to achieve compact and efficient energy transfer (see Fig. 3(a)). A numerical study on a Si wire to SSW orthogonal junction has previously been performed [16]; however, without the angled facet, there is minimal spatial overlap between the two waveguides such that only the evanescent field in the air claddings of the Si wire would couple into the SSW despite the matching momenta. The angled facet increases the spatial overlap by enhancing the magnitude of the evanescent field and also serves as a reflector that redirects a fraction of the EM power residing in the Si wire core towards the SSW. Furthermore, the angled surface ensures that the total internal reflection condition is still satisfied through the bend. Thus, the length and position of the facet (offset from the outer cladding of the SSW) together determine the spatial modal overlap between the two waveguides and are important design parameters for the orthogonal coupler. For a proof-of-concept demonstration, an orthogonal bend operating near 1300 nm is designed and then experimentally implemented and characterized. Using a commercial mode solver from Lumerical and taking into account that the design will be fabricated on a silicon-on-insulator (SOI) platform with Si thickness of 220 nm, it is calculated that phase matching between $k_{t,\mathrm{Si}}$ and $k_{\mathrm{l,SSW}}$ can be achieved at 1288 nm using a

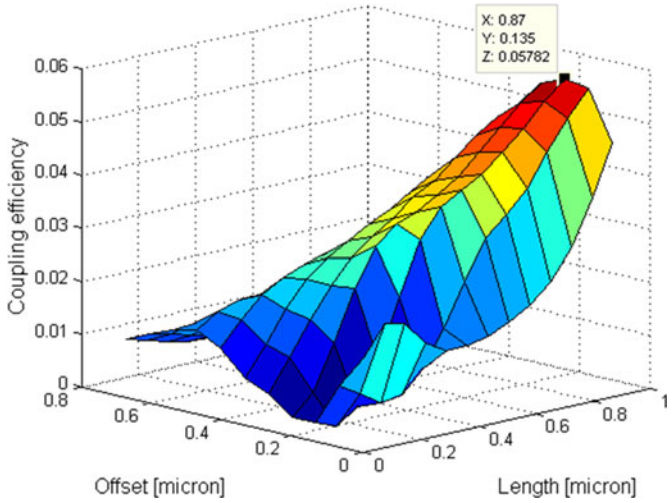

Fig. 4. 3-D isometric plot of coupling efficiency from Si wire to the SSW slot region as a function of length and offset of the angled facet. The maximum coupling efficiency occurs at an angled facet length of 0.87 μm and an offset of 0.135 μm.

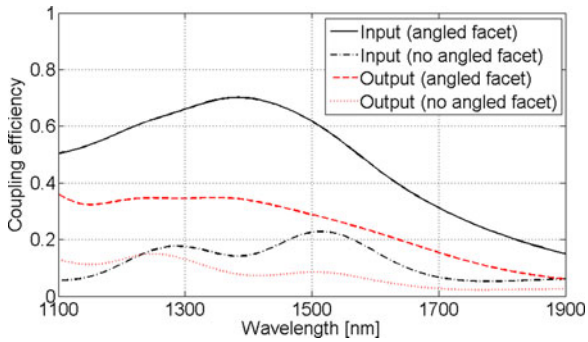

Fig. 5. Plots of coupling efficiencies of input Si wire to SSW orthogonal bends with and without angled facet, and output SSW to Si wire orthogonal bends with and without angled facet.

500 nm Si wire and a SSW with 300 nm claddings and 130 nm gap (see Fig. 2(a)). The 130 nm slot is chosen since that is the minimum resolution achievable by the fabrication technology available to us. With these dimensions, the waveguides support only the fundamental TE modes at 1288 nm.

The SSW can support both the symmetric and antisymmetric supermodes of the two silicon claddings waveguide system. The orthogonal coupler demonstrated in this work couples to both the symmetric and antisymmetric modes of the SSW. Since the symmetric mode, also referred to as the slot mode, has an appreciable portion of power residing in the slot region, it is responsible for the field enhancement effect; whereas the antisymmetric mode that is also supported has power mostly contained within the silicon claddings. Using 3-D FDTD simulation software by Lumerical, the design of an orthogonal junction with waveguide dimensions specified above is optimized for maximum coupling efficiency to the slot mode of the SSW. First, optimization of the amount of power residing within the SSW slot region is performed by sweeping the length of the angled facet from 0 to 1000 nm and the offset from 0 to 800 nm. The optimal angled facet dimensions are determined to be 870 nm in length and 135 nm in offset (see Fig. 4). To ensure that the parameters of the orthogonal junction optimized for maximum coupling to the slot mode is not very far from the parameters optimized for overall coupling efficiency to the SSW, which would be detrimental for the coupler design, the coupling efficiency into the entire SSW, including the power within the Si claddings, is maximized. The optimization results show that by decreasing the angled facet length to 725 nm, high SSW coupling efficiency is achieved with only a slight decrease in power coupling to SSW slot region. The optimization maximized the overall power coupled to the SSW, but it is found that the power coupled into the slot mode using the same angled facet parameters is close to maximum. As a result, the orthogonal coupler design has an angled facet length of 725 nm and is located 135 nm away from the outer-cladding of the SSW (see Fig. 3(a)). Fig. 5 shows that the implementation of the angled facet leads to almost a threefold magnification in coupling efficiency of the Si wire–SSW junction. Peak coupling efficiency of around 70% and a 3-dB bandwidth of over 500 nm are achieved through the orthogonal coupler that occupies only 725 nm $\times$ 500 nm. The footprint of the orthogonal coupler is based on the right-angled triangle that the tilted facet forms, with perpendicular sides of length 725 nm (length of angled facet) and 500 nm (width of Si wire), as shown in Fig. 3(a). The wavelength of peak coupling efficiency offsets from the phase matching wavelength of 1288 nm as shown in Fig. 2(a), because the angled facet represents a modification of the ideal orthogonal configuration of the Si wire to SSW interface. On the other hand, by including the same optimized angled facet, the coupling efficiency of a SSW–Si wire junction is also significantly improved and reaches $\sim$40%, even though this is lower than that of a Si wire–SSW junction (see Fig. 5). The coupling efficiencies for the input and output couplers are different, because in the simulation of the output coupler, only the symmetric mode is launched into the SSW, whereas the Si wire mode excites both symmetric and antisymmetric modes of the SSW through the input coupler. As such, if both the symmetric and antisymmetric modes, with the same power ratio as excited by the input coupler, is launched into the SSW, then the transmission of the output coupler would be the same as that of the input coupler. On the other hand, different angled facet parameters are required for optimizing efficient redirection of modal energy for the SSW–Si wire junction if only the symmetric mode is launched into the SSW.

Finally, the transmission response of a SSW orthogonal coupling platform that includes both Si wire to SSW input bend and SSW to Si wire output bend is shown in Fig. 7. Separate simulations for the input and output bends are performed and the spectra are multiplied to yield the transmission response of the overall coupling platform. This is used as a reference for comparing with experimental transmission results for the orthogonal coupling platform, as the transmission or cutback measurements will not allow us to resolve the coupling efficiencies of the input and output bends separately and can only provide us with the overall transmission of light going through both junctions.

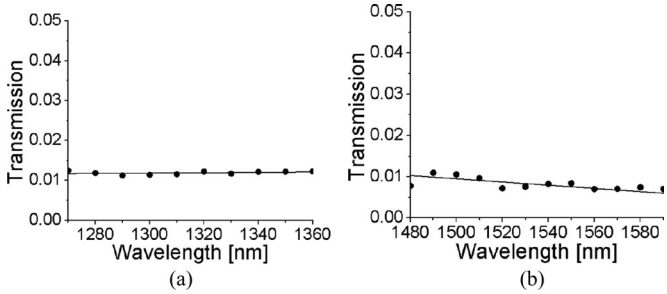

Fig. 6. Plots of transmission of Si wire waveguide in the wavelength ranges from (a) 1270 to 1360 nm and from (b) 1480 to 1590 nm.

III. Experimental Realization of the 90° Bend

To experimentally demonstrate the performance of our 90° bend, the optimized design shown in Fig. 3(a) is fabricated on SOI wafer with 220 nm top Si layer. The waveguides are patterned using 193 nm deep UV lithography, 130 nm mask technology, and inductively coupled plasma reactive ion etching. A scanning electron microscope (SEM) image of the fabricated structure is shown in Fig. 3(b). The bandwidth of the bend is demonstrated by performing transmission measurements in two wavelength regimes: from 1270 to 1360 nm and from 1480 to 1590 nm. A standard end-fire coupling rig is used with input coupling to the edge of the sample from a tapered tip optical fiber and the output light collected with a microscope objective lens. At the sample edge, the width of the Si wire is 2 μm, which is tapered down to 500 nm before reaching the orthogonal coupler to the SSW. The transmission of the Si wire–SSW coupling platform is first measured and then normalized to that of a nearby straight Si wire to isolate the performance of the bends. The transmission of the Si wire waveguide for the wavelength ranges from 1270 to 1360 nm and from 1480 to 1590 nm are shown in Fig. 6, which includes the input and output coupling, and also the propagation loss within the Si wire, and thus it represents the total insertion loss of the waveguide. Measurements are carried out on many Si wire waveguides on the sample, with the transmission for the different waveguides varying from 0.7% to 1.3%. Fig. 6 shows the average of the transmission of these Si wire waveguides. The low transmission of the Si wire waveguide (high insertion loss) is predominantly due to input coupling loss, because there is a large spatial mode mismatch between the input fiber tip Gaussian beam and the highly elongated elliptical mode of the Si wire at the edge of the sample that is 2 μm in width and 220 nm in height.

Given that the propagation loss in a SSW is close to 10 dB/cm in the characterized wavelength regimes [6] and the longest SSW in the fabricated samples is 50 μm, optical power is only attenuated by less than 2% within the SSW section. This means the insertion loss of the fabricated orthogonal coupler is dominated by the input and output coupling losses. Thus, it is a valid approximation to compare the measured spectrum directly to the simulation result, which does not include the intermediate SSW section. However, it should be noted that the various waveguide interfaces will induce reflections and hence create resonance features in the measured spectrum. Nonetheless, from Fig. 7, it

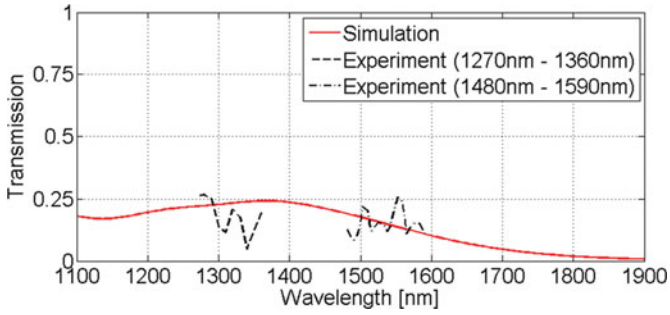

Fig. 7. Plots of multiplication of the simulated transmissions of the input Si wire to SSW and output SSW to Si wire orthogonal bends, and the experimental transmission of the Si wire to SSW orthogonal coupling platform, as a function of wavelength.

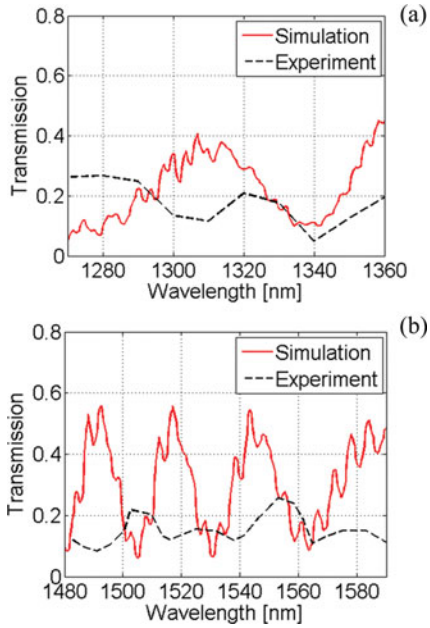

Fig. 8. Plots of the simulated and experimental transmissions of the Si wire to SSW orthogonal coupling platform as a function of wavelength in the range (a) from 1270 nm to 1360 nm and (b) from 1480 nm to 1590 nm.

can be observed that the nominal values of the experimental data match closely with simulated results: in the 1270 to 1360 nm range, the average experimental and simulated transmissions are 18% and 23%, respectively; and in the 1480 to 1590 nm range, the average experimental and simulated transmissions are 14% and 15%, respectively.

In order to verify that the resonances in the measured data are due to the SSW section, an additional 3-D FDTD simulation is performed that includes the 50 μm SSW section, which represents the actual orthogonal coupling platform. It can be seen in Fig. 8(a) and (b) that resonances with similar periods are present in the 1270 to 1360 nm and 1480 to 1590 nm wavelength ranges, respectively. This confirms that the SSW section is in fact the cause of the observed resonances.

In the simulation result, there are actually two distinct resonance features, namely the smaller period fringes and the large envelope fringes. Here we show that the smaller period fringes are caused by the SSW acting as a Fabry–Perót cavity, and

the large envelop fringes are due to the beating between the quasi-TE symmetric and antisymmetric supermodes of the two coupled waveguides (Si claddings) that form the SSW. This is because the Si wire fundamental quasi-TE mode actually couples to both fundamental quasi-TE modes of the SSW through the 90° bend, and the mode with higher optical power concentrated in the slot region is the symmetric mode. To calculate the period of the smaller fringes, the group index (n_g) of the quasi-TE symmetric mode of the SSW is deduced from dispersion data obtained from simulations using the mode solver by Lumerical Inc. It is essentially the free spectral range (FSR) of the SSW cavity, which is given by: FSR $= \lambda^2 / (2n_g \mathrm{L})$, where λ is the wavelength and L is the length of the SSW. Around $\lambda =$ 1300 nm, n_g is approximately 4.78, which results in FSR $\sim$ 3.5 nm; and near $\lambda = 1550$ nm, n_g is approximately 3.93, which results in FSR $\sim$ 6.1 nm. These FSR values compare quite well to that of the 3-D FDTD simulation shown in Fig. 8. In order to calculate the larger envelop fringe period ($\Delta\lambda$), the group index of the quasi-TE antisymmetric mode of the SSW must also be known. The fringe period due to the beating of two modes is given by: $\Delta\lambda = \lambda^2 / (\Delta n_g L)$, where Δn_g is the difference in group index of the two modes. Using a mode solver, the group indices of the quasi-TE antisymmetric modes of the SSW at the wavelengths of 1300 nm and 1550 nm are 5.29 and 2.95, respectively. From these values of group indices, the large envelop fringe period near $\lambda = 1300$ nm is calculated to be $\Delta\lambda \sim 66.3$ nm; and near $\lambda = 1550$, it is $\Delta\lambda \sim 49.0$ nm. The large envelop fringe period near 1300 nm compares very well to the simulation result in the range from 1270 to 1360 nm, as shown in Fig. 8(a). However, in the range from 1480 to 1590 nm (see Fig. 8(b)), the calculated fringe period does not compare as well to the simulation result, although they are still on the same order of magnitude. It is noted that the fringes in the experimental data represent the effect of beating between the quasi-TE symmetric and antisymmetric modes of the SSW, while the fringes due to multiple reflections within the SSW cavity are not resolved because more closely spaced data points in wavelength would be required in the measurements.

To measure the SSW propagation loss and further verify the results obtained from the preceding experimental method, the cut-back method is carried out by measuring transmission as a function of SSW length for three different wavelengths: 1450, 1550, and 1650 nm. Multiple devices that contain SSW of the same length are measured to generate the error bar and the results are shown in Fig. 9(a). By performing a linear fit of logarithmic transmission as a function of SSW length, the propagation loss of (or transmission within) the SSW can be obtained from the slope of the respective fit, and the multiplication of input and output coupling efficiencies can be calculated from the intercept on the $\log(T)$ axis. It is measured that the transmissions within a 50 μm length SSW are approximately 55%, 72%, and 86%, for the wavelengths of 1450 nm, 1550 nm, and 1650 nm, respectively. Also, the multiplication of input and output coupling efficiencies are determined to be approximately 17%, 21%, and 3%. Finally, by multiplying the transmission within the SSW and the input and output coupling efficiencies, the overall transmissions of approximately 9.2%, 15.4%, and 2.5% are obtained (see Fig. 9(b)). Indeed, in comparison to Fig. 7, these values match closely with simulation results: from 1450 to 1550 nm, the average simulated transmission of the SSW is around 15%, and near 1650 nm, it is approximately 8%. The deviation of experimental result from simulation study can be attributed to fabrication imperfections. For example, sidewall roughness would lead to appreciable propagation loss within the SSW not accounted for in simulation, and the trapezoidal Si waveguide cross-section and rounded waveguide corners (see Fig. 3(b)) can alter the waveguide effective indices and thus affect the phase matching condition and induce scattering loss.

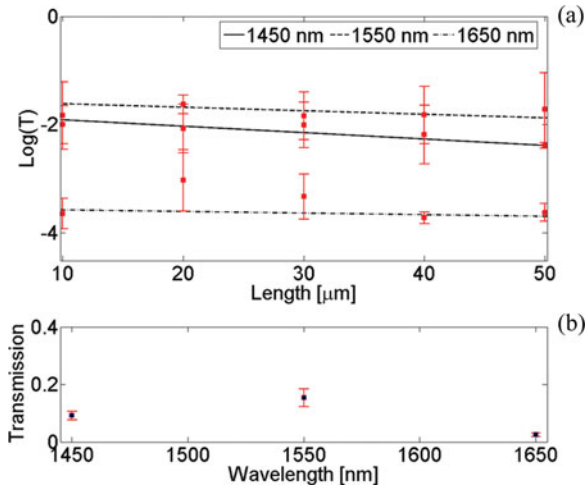

Fig. 9. (a) Linear fits of the logarithm of transmission $\log(T)$ as a function of SSW length for the wavelengths of 1450 nm, 1550 nm, and 1650 nm. (b) Overall transmission of Si wire to SSW coupling platform as a function of wavelength.

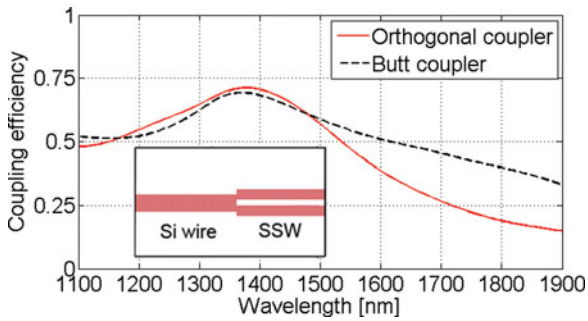

Fig. 10. Plots of coupling efficiencies of the Si wire to SSW butt coupler and orthogonal bend as a function of wavelength.

IV. Device Performance and Sensitivity Analysis

The 90° waveguide bend from Si wire to SSW is a component that will serve to increase the integration density of on-chip photonic devices, because it allows for a change in light propagation direction from one waveguide to another with minimal space requirements. As such, its performance must be compared to the butt (parallel) coupler from Si wire to SSW (inset of Fig. 10), which is the baseline case when the direction of propagation is not altered. 3-D FDTD simulation is performed on one butt coupler junction from Si wire to SSW, and the coupling efficiency is shown in Fig. 10. It can be seen that the 90° bend (orthogonal

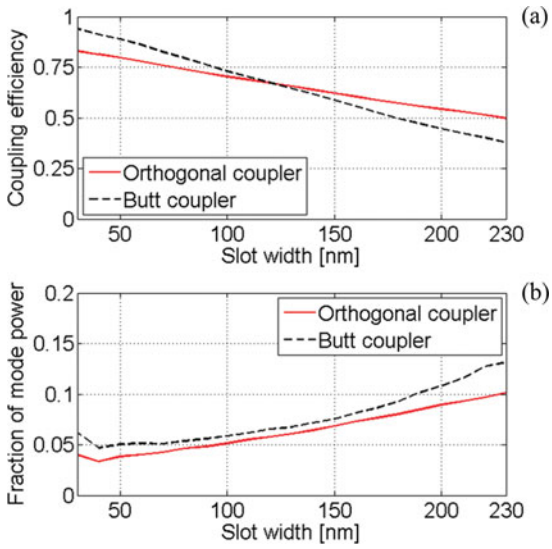

Fig. 11. (a) Plots of coupling efficiency of the 90° bend and the butt coupler from Si wire to SSW as a function of slot width at the wavelength of 1300 nm. (b) Plots of fraction of mode power within the slot region for coupling with the 90° bend and butt coupler from Si wire to the SSW as a function of slot width at the wavelength of 1300 nm.

coupler) designed in this work has a similar spectral transmission profile as the butt coupler, and only has significantly lower transmission for wavelengths above 1600 nm. This confirms that our design methodology for the orthogonal bend is capable of achieving transmission characteristics approaching that of direct butt coupling.

A sensitivity analysis is performed by varying the slot width while keeping the Si cladding width of the SSW and the angled facet dimensions constant. As seen in Fig. 11(a), the coupling efficiency from the Si wire to the SSW at the wavelength of 1300 nm (wavelength at which the 90° bend is designed for) decreases when the slot width is increased from 30 to 230 nm, in both the orthogonal bend and the butt coupling configuration. The decrease in coupling efficiency is more pronounced for the butt coupler, which means that the orthogonal bend is slightly less sensitive to changes the SSW slot width. An explanation for Fig. 11(a) is that as the slot width is increased, the effective index of the SSW mode deviates more from the effective index of the Si wire mode, leading to increased phase and modal mismatches that decreases coupling efficiency. From Fig. 11(b), it can be seen that at the same wavelength of 1300 nm, as the SSW slot width is increased from 30 to 230 nm, the fraction of mode power inside of the slot region is more than doubled, for both the orthogonal bend and the butt coupler. This is because as the two Si claddings of the SSW are moved apart, more power would reside within the larger slot region in between. Over the range of slot widths studied, the fraction of mode power within the slot region varies from $<5\%$ to $>12\%$ (Fig. 11(b)), which is consistent with the value of $\sim 8.4\%$ obtained from the Lumerical mode solver for the SSW with 300 nm Si claddings and 130 nm slot width. Note that while the fraction of mode power is quite low hovering near 10%, the fraction of electric field intensity within the slot region is at around 30%. Fig. 11 shows that while the coupling efficiency into the overall SSW is similar for the orthogonal bend and the butt coupler, slightly less power is coupled into the slot mode (TE symmetric mode) of the SSW for the orthogonal bend over the entire range of slot widths. This further supports the hypothesis that the orthogonal bend from Si wire also excites the TE antisymmetric mode of the SSW, whereas the butt coupler only excites the TE symmetric mode.

V. Conclusion

We have experimentally demonstrated the proof-of-concept of a Si wire-to-slot waveguide 90° bend that has theoretical 3-dB bandwidth of over 500 nm, peak efficiency of around 70%, and a footprint of ~ 725 nm $\times$ 500 nm. Through momentum matching via orthogonal waveguide placement, coupling characteristics comparable to that of direct butt coupler is achieved. The experimental data matches well with simulation results, and the device can be further improved by optimizing the parameters of the output bend. Overall, the orthogonal bend configuration presented can lead to more densely integrated silicon photonic circuits containing devices and interconnects that utilize both the Si wire and slot waveguides.

References

[1] V. R. Almeida, Q. Xu, C. A. Barrios, and M. Lipson, "Guiding and confining light in void nanostructure," *Opt. Lett.*, vol. 29, pp. 1209–1211, 2004.

[2] A. Martinez, J. Blasco, P. Sanchis, J. Galán, J. García-Rupérez, E. Jordana, P. Gautier, Y. Lebour, S. Hernández, R. Spano, R. Guider, N. Daldosso, B. Garrido, J. M. Fedeli, L. Pavesi, and J. Martí, "Ultrafast all-optical switching in a silicon-nanocrystal-based silicon slot waveguide at telecom wavelengths," *Nano Lett.*, vol. 10, pp. 1506–1511, 2010.

[3] T. Baehr-Jones, M. Hochberg, G. Wang, R. Lawson, Y. Liao, P. Sullivan, L. Dalton, A. Jen, and A. Scherer, "Optical modulation and detection in slotted silicon waveguides," *Opt. Exp.*, vol. 13, pp. 5216–5226, 2005.

[4] J. T. Robinson, L. Chen, and M. Lipson, "On-chip gas detection in silicon optical microcavities," *Opt. Exp.*, vol. 16, pp. 4296–4301, 2008.

[5] D. Erickson, X. Serey, Y. F. Chen, and S. Mandal, "Nanomanipulation using near field photonics," *Lab Chip*, vol. 11, pp. 995–1009, 2011.

[6] T. Baehr-Jones, M. Hochberg, C. Walker, and A. Scherer, "High-Q optical resonators in silicon-on-insulator-based slot waveguides," *Appl. Phys. Lett.*, vol. 86, pp. 081101-1–081101-3, 2005.

[7] M. Gnan, S. Thoms, D. S. Macintyre, R. M. De La Rue, and M. Sorel, "Fabrication of low-loss photonic wires in silicon-on-insulator using hydrogen silsesquioxane electron-beam resist," *Electron. Lett.*, vol. 44, no. 2, pp. 115–116, 2008.

[8] N. N. Feng, R. Sun, L. C. Kimerling, and J. Michel, "Lossless strip-to-slot waveguide transformer," *Opt. Lett.*, vol. 32, pp. 1250–1252, 2007.

[9] N. N. Feng, R. Sun, J. Michel, and L. C. Kimerling, "Low-loss compact-size slotted waveguide polarization rotator and transformer," *Opt. Lett.*, vol. 32, pp. 2131–2133, 2007.

[10] Z. Wang, N. Zhu, Y. Tang, L. Wosinski, D. Dai, and S. He, "Ultracompact low-loss coupler between strip and slot waveguides," *Opt. Lett.*, vol. 34, pp. 1498–1500, 2009.

[11] Y. Liu, T. Baehr-Jones, J. Li, A. Pomerene, and M. Hochberg, "Efficient strip to strip-loaded slot mode converter in silicon-on-insulator," *IEEE Photon. Technol. Lett.*, vol. 23, no. 20, pp. 1496–1498, 2011.

[12] P. A. Anderson, B. S. Schmidt, and M. Lipson, "High confinement in silicon slot waveguides with sharp bends," *Opt. Exp.*, vol. 14, pp. 9197–9202, 2006.

[13] S. K. Selvaraja, W. Bogaerts, and D. V. Thourhout, "Loss reduction in silicon nanophotonic waveguide micro-bends through etch profile improvement," *Opt. Commun.*, vol. 284, pp. 2141–2144, 2011.

[14] B. Lau, M. Swillam, and A. S. Helmy, "Hybrid orthogonal junctions: wideband plasmonic slot-silicon waveguide couplers," *Opt. Exp.*, vol. 18, pp. 27048–27059, 2010.

[15] C. Lin, H. Wong, B. Lau, M. Swillam, and A. S. Helmy, "Efficient broadband energy transfer via momentum matching at hybrid junctions of guided-waves," *Appl. Phys. Lett.*, vol. 101, pp. 123115-1–123115-4, 2012.
[16] F. Li, X. Hu, J. Wu, L. Zhou, and Y. Su, "Ultra-compact and broadband orthogonal coupler between strip and slot silicon waveguides," *Proc. SPIE*, vol. 8307, pp. 83070B-1–83070B-6, 2011.

Herman M. K. Wong received the B.A.Sc. degree from the Division of Engineering Science, with specialization in nanoengineering, in 2008 and the M.A.Sc. degree from the Department of Electrical and Computer Engineering with a focus on integrated photonics and plasmonics in 2011, both from the University of Toronto, ON, Canada, where he is currently working toward the Ph.D. degree in the Photonics Group, Department of Electrical and Computer Engineering. He is currently a Graduate Research Intern at Intel Labs in Santa Clara, CA, USA, working on the characterization of silicon photonic devices. He completed an internship at the Institute of Photonic Sciences in Barcelona, Spain in 2009, conducting research on surface plasmon-based optical tweezers. His research interests include plasmonic devices and systems, silicon photonics, and their applications to optical communications and sensing.

Charles Lin received the B.A.Sc. degree in 2010 and the M.A.Sc. degree in 2012, both in electrical engineering from the University of Toronto, where he is currently working toward the Ph.D. degree in photonics. His research interests include plasmonic resonance and field effects, plasmonic waveguiding structures, and nanoplasmonic devices and applications.

Mohamed A. Swillam received the Ph.D. degree from McMaster University, Hamilton, Canada, in 2008. After graduation, he worked as a Postdoctoral fellow in the same group. In October 2009, he joined the Photonics Group and the Institute of Optical Sciences at the University of Toronto where he currently works as a Research Fellow. In September 2011, he was appointed as an Assistant Professor at the Department of Physics, the American University in Cairo (AUC), Cairo, Egypt. His research interests include active and passive nanophotonic and plasmonic devices and systems, silicon photonics, optical interconnects, integrated optical systems and lab on chip, and solar cells. He authored more than 80 technical papers in highly ranked journals and conferences in these areas. He is a member of the editorial board of many physics and photonics journals. He is also a senior member of the IEEE Photonics Society. He is the Founder and the Advisor of the Optical Society of America chapter in the AUC and the Vice-President of the Egyptian Unit. He received various awards and fellowships including Misr Elkhair best publication award in 2012, NSERC postdoctoral fellowship 2009, and the Dean's graduate student award of knowledge translation and innovation from McMaster University in 2009. He also won the competition for Ontario Ministry of Research fellowship round 5 for 2011. He also received the best student paper award from IEEE/LEOS Ottawa section for Photonics North 2007 and from ACES 2009.

Amr S. Helmy received the B.Sc. degree in electronics and telecommunications engineering from Cairo University in 1993, the M.Sc. and Ph.D. degrees from the University of Glasgow with a focus on photonic devices and fabrication technologies, in 1999 and 1995, respectively. He is currently a Professor in the Department of Electrical and Computer Engineering, University of Toronto. Prior to his academic career, he held a position at Agilent Technologies photonic devices, R&D division, U.K. between 2000 and 2004. His research interests include photonic device physics and characterization techniques, with emphasis on nonlinear optics in III–V semiconductors, applied optical spectroscopy in III–V optoelectronic devices and materials, III–V fabrication and monolithic integration techniques.